DFT STUDY OF THE KINETICS OF CHEMICAL TRANSFORMATION OF COBALT TO COBALT OXIDES AND SULFIDES

A Thesis

Presented to the Faculty of the Graduate School

of Cornell University

In Partial Fulfillment of the Requirements for the Degree of

Master of Science

by

Shreyas Jaikumar Honrao

May 2013

ABSTRACT

DFT was used to study the chemical transformation of ε-Co into its oxides and sulfides. Defect formation energies and migration barriers were calculated to determine the diffusion activation energies. Combining these results with experimental data allowed us to elucidate the dominant diffusion mechanisms in these systems.

It was found that transformation from ε-Co to CoO occurs *via* an indirect-exchange mechanism, with Co atoms diffusing outwards and O atoms diffusing inwards. Once CoO forms, the mechanism changes; Co atoms diffuse outwards faster, forming a void inside.

We looked at the Co-N, Co-F and Co-S systems to study the exciting indirect-exchange mechanism in greater detail. Our observations helped us explain the mechanism lucidly, and predict that such a mechanism might be active in Co-N as well.

We also studied an interesting anion-exchange reaction. We observed that Co and O atoms diffuse outwards, while S atoms hardly move, as CoO NPs transform to Co_3S_4.

BIOGRAPHICAL SKETCH

Shreyas Jaikumar Honrao was born March 16, 1990 in Mumbai, India. He received the Bachelor of Technology from IIT Madras in 2011. His decision to attend Cornell University for his graduate studies took him from the hottest city he had lived in to the coldest place he ever hoped to stay at. He has been awarded a number of prestigious scholarships and awards during his academic career, noteworthy among which are the National Talent Search scholarship and the J. N. Tata scholarship for graduate studies. Most of his recent work is in the field of computational materials science, but he has previous experience on the experimental side too. When not studying or working on research, he is most likely to be found playing soccer, cooking, reading or solving puzzles!

To Aai and Papa, who have always believed in both of us.

ACKNOWLEDGMENTS

I am very grateful to my advisor, Richard Hennig, for his guidance, patience and the encouragement he has shown me. Thank you for having an answer to every trivial doubt or question I had. Also, thanks to Richard Robinson, who was almost like a second advisor to me. Thank you for giving me a chance to collaborate with your excellent team of researchers.

I would like to acknowledge all of my lab mates for helping me from time to time; Don and Haitao, especially, for the valuable things I was able to learn from them. I also want to say thank you to XSEDE for their brilliant computational resources that I have been using over the past two years.

Finally, I would like to thank my friends, Ved, Chaitanya, Anuja, Rohil, and so many more, for supporting me throughout. And obviously, to my biggest source of inspiration, my twin brother, Chinmay.

TABLE OF CONTENTS

LIST OF FIGURES

LIST OF TABLES

LIST OF ABBREVIATIONS

NP	Nanoparticle
MD	Molecular Dynamics
DFT	Density Functional Theory
HCP	Hexagonal close-packed
FCC	Face-centered cubic
XRD	X-Ray Diffraction
XAS	X-Ray Absorption Spectroscopy
TEM	Transmission Electron Microscopy
NEB	Nudged Elastic Band
MEP	Minimum Energy Path
PAW	Projector Augmented Wave
VASP	Vienna Ab-initio Simulation Package
HSAB	Hard Soft Acid Base
EXAFS	Extended X-Ray Absorption Fine Structure
ICP-MS	Inductively Coupled Plasma Mass Spectrometry
HRTEM	High Resolution Transmission Electron Microscopy

CHAPTER 1

INTRODUCTION

Characterization of nanoparticles (NPs) is a unique problem. Their small size and the importance of their surfaces pose a problem to both experimental and theoretical scientists. The high surface to volume ratio, further, makes knowledge of the structure of the near-surface layers necessary. A combination of experimental and computational methods can provide the necessary insights into the atomic structure, thermodynamic stability, kinetics of diffusion and phase transformations of NPs. Experimental methods based on X-rays and electron microscopy can provide important structural information. Computational studies such as density functional theory (DFT) calculations, on the other hand, can provide information about the energetics and atomistic structures of nanocrystals, point defects, diffusion barriers, and surfaces. Knowledge about the transformation mechanisms and structural properties provides a means to control the synthesis and composition of the NPs and facilitate the optimization of such NPs for use in applications.

1.1 Motivation

Most of the chemical transformations in bulk systems can be described using thermodynamic stability and kinetic aspects of diffusion, nucleation and growth, and it is often possible to predict the likely mechanism of reactions and phase transformations. However, this changes as we go to the nanoscale. Properties like surface area come into picture, and these systems display interesting and unexpected transformation kinetics.[1–3] As a result, characterizing these systems becomes a major problem for materials scientists. A more complete understanding of the transformation pathways would

enable the prediction of the unique products resulting from chemical transformations of NPs.

1.2 Atomic view of diffusion

Diffusion in solids takes places by various mechanisms that often involve defects, e.g. the substitutional or the interstitial mechanism illustrated in Fig. 1.1. In order for an atom to diffuse to the adjacent vacant or interstitial site, it needs to overcome a potential energy (or activation) barrier.

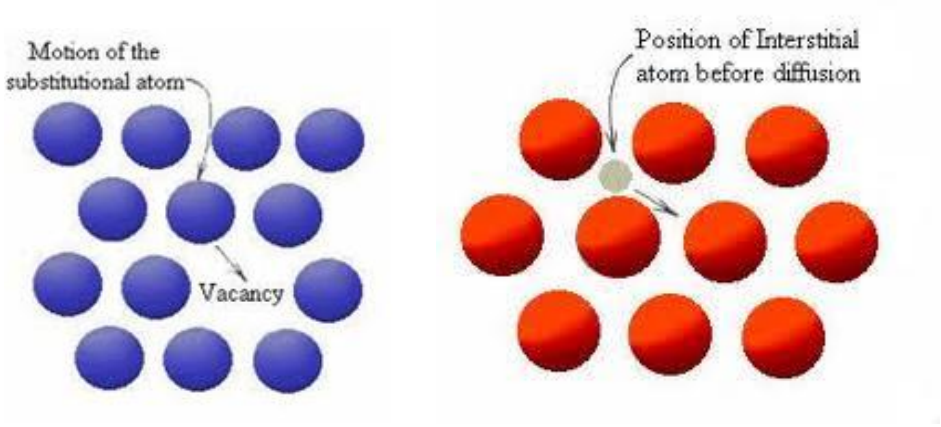

Figure 1.1. Schematic representation of vanacany diffusion (left) and interstitial diffusion (right).[4]

The flux in one direction can then be given by the following equation -

$$J_{1-2} = \frac{1}{6}\nu\left[e^{-E_f / kT}\right]\left[e^{-E_j / kT}\right](Ca_o)$$

can jump in any direction in cubic lattice

jump attempt frequency

probability of a vacancy nearby

activation energy barrier

number of atoms available per unit area

There is a similar flux in the opposite direction. Adding both these terms gives us the net flux.

$$J_{net} = J_{1-2} - J_{2-1} = -\left[\frac{1}{6}a_o^2\nu\right]\left[e^{-(E_f+E_j)/kT}\right]\frac{dC}{dx}$$

Comparing this to Fick's fist law gives -

$$D = D_{\circ} e^{-E_D / kT}$$

where

$$D_{\circ} = \frac{1}{6} a_{\circ}^2 \nu \quad .$$

Thus, using the jump frequency, we can calculate the diffusion constant in a material.

1.3 The Kirkendall effect

The Kirkendall effect is a classical phenomenon in metallurgy, arising from the different diffusivities of two components in an alloy, when diffusion of both species occurs by a vacancy mechanism. When one of the species diffuses at a faster rate than the other, the net directional flow of matter is balanced by an opposite flow of vacancies. The net vacancy flux leads to the formation of voids on one side of the material, whose annihilation results in the shrinking of the material. One the other side of the material, the removal of vacancies results in the creation of new vacancies and the swelling of the material.

For NPs, the Kirkendall effect can be utilized to synthesize hollow nanostructures. Considerable progress has recently been made in synthesizing colloidal nanocrystals with well-controlled size, shape, and surface properties making use of this effect. [1,2] One of the main advantages of the Kirkendall effect is that it gives rise to highly crystalline hollow NPs, even in the quantum regime. Furthermore, compared to many multistep organic chemical fabrication routes, which usually need further purification processes, the Kirkendall effect provides a one-pot mass synthesis route to materials with nearly 100% purity.[2]

1.4 Cobalt

Cobalt is a transition metal that exhibits in bulk phase two allotropic forms: the hexagonal close-packed (HCP) structure which is stable below 417°C, and the face-centered-cubic (FCC) structure which is stable at higher temperatures. Cobalt is one of the three metals that are ferromagnetic at room temperature.[5] It is ferromagnetic up to 1,121°C, the highest known Curie point of any metal or alloy,[6] and hence has applications where magnetic properties are needed at elevated temperatures. It dissolves slowly in dilute mineral acids, does not react directly with either hydrogen or nitrogen, but will react, on heating, with carbon, phosphorus, or sulfur. Cobalt is also attacked by oxygen and by water vapor at elevated temperatures forming cobalt monoxide, CoO.[6]

At the nanoscale, however, cobalt sometimes forms in the cubic ε-Co phase with space group #212.[7] The ε-Co unit cell has 20 atoms. Based on their Wyckoff positions within the unit cell, 8 of the sites are classified as type I, and 12 are type II (Fig. 1.2).

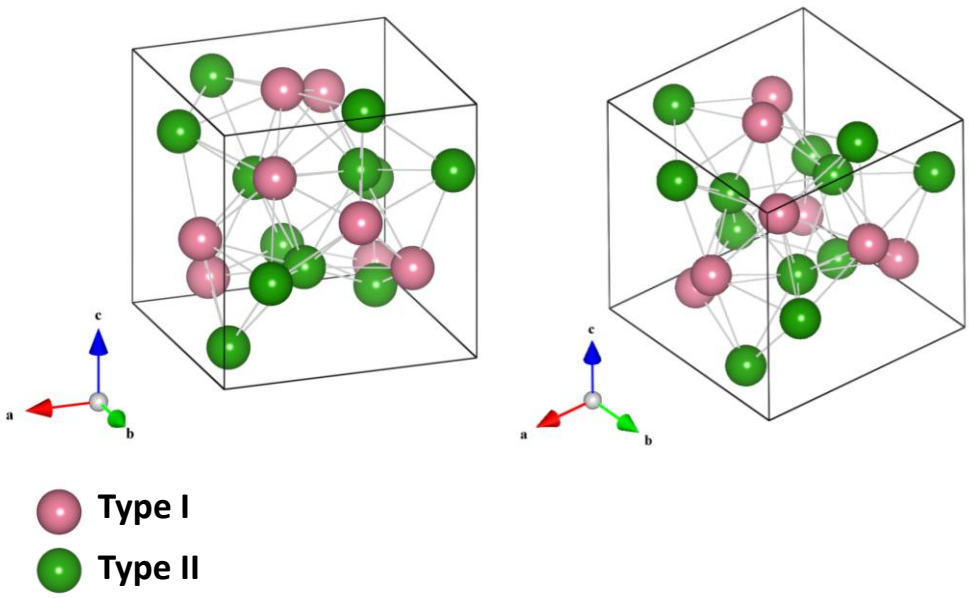

Figure 1.2. The crystal structure of ε-cobalt. The pink and green atoms represent the type I and II cobalt atomic positions, respectively.

1.5 Research objectives

In this project we use DFT to study the thermodynamics, kinetics and diffusion processes involved in the transformations that take place as ε-Co is converted to its oxides and sulfides. The calculated defect formation energies and migration barriers will be used to determine the diffusion activation energies. Comparing these activation energies will give help us elucidate the dominant diffusion mechanism in these systems.

This project is carried out in collaboration with the experimental group of Prof. Richard Robinson, who synthesized and characterized these colloidal NP systems. Experimental techniques like X-ray diffraction (XRD), X-ray absorption spectroscopy (XAS) and transmission electron microscopy (TEM) are used to characterize the intermediate steps and products of these reactions.

We combine our theoretical results on the diffusion processes and kinetics with experimental data on the structural changes involved in the transformation, to determine the most probable mechanisms of these reactions. Such a process will help us study these systems in a greater detail than has been achieved in previous studies. Knowledge about the transformation method and structural properties will provide materials scientists with a means to control the synthesis and composition of these NPs and facilitate their optimization in applications.

CHAPTER 2

METHODS

2.1 Density functional theory

Density-functional theory (DFT) provides an efficient tool to compute the ground state energy of materials.[8,9] It is based on the concept that the total energy, E, of an electronic system is a functional of the ground-state electron density, ρ. DFT is presently the most successful (and also the most promising) approach to compute the electronic structure of materials. Its applicability ranges from atoms, molecules and solids to nuclei and quantum and classical fluids. DFT predicts a great variety of molecular properties: molecular structures, vibrational frequencies, atomization energies, ionization energies, electric and magnetic properties, reaction paths, etc. Typically, DFT calculations are carried out at 0 K. However, over the past few years, the original DFT has been generalized to deal with many different situations: spin polarized systems, free energy at finite temperatures, molecular dynamics, etc.

2.1.1 VASP

We use the Vienna Ab-initio Simulation Package, better known as VASP,[10–13] for performing all our ab-initio quantum mechanical calculations. VASP is a software package based on DFT, but the code also provides methods beyond DFT such as hybrid functionals, many-body perturbation theory (the GW method), and dynamical electronic correlations within the random phase approximation. VASP usually makes use either of Vanderbilt-type ultrasoft pseudopotentials,[14–16] or the projector augmented wave method,[17,18] and a plane wave basis set.

2.2 Calculation of diffusion activation barriers

Most mechanisms for diffusion rely on the formation of point defects and the motion of atoms via these defects. These defects include vacancies, interstitials, or substitutional atoms. The energy required for forming the point defects – the defect formation energy E_{def}^{f} – controls the concentration of the defects. Diffusion occurs when the defect migrates from one site to an adjacent site. In order for a defect to move to another site, it needs to overcome a potential energy barrier, also called as the defect migration energy barrier, E_{def}^{m} (Fig. 2.1).

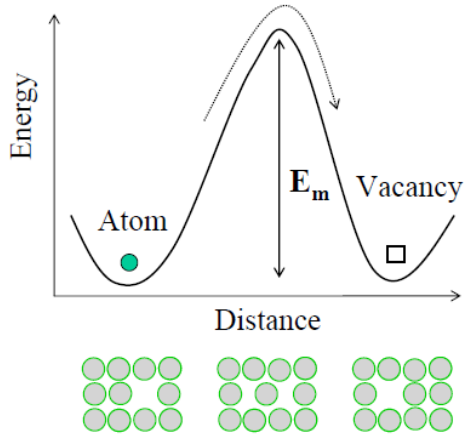

Figure 2.1. Schematic representation of the diffusion of an atom from its original position into a vacant lattice site.[19]

For a defect-mediated diffusion mechanism, the activation energy of diffusion, E_{def}^{act}, is given by the sum of the defect formation energy, E_{def}^{f}, and the defect migration energy barrier, E_{def}^{m}.

$$E_{def}^{act} = E_{def}^{f} + E_{def}^{m}$$

To study relative diffusivities of the different species, we calculate diffusion activation barriers for each of them. Formation energies and migration barriers are calculated using DFT within the VASP code. The energy barrier to migration of the diffusing species, E_{def}^{m}, is calculated using the nudged elastic band (NEB) [20] method (see Sec.

2.2.1). Adding these two energies gives us the final diffusion activation barrier, $E_{\text{def}}^{\text{act}}$, for that species and diffusion mechanism. Comparing the activation barriers for competing mechanisms and species of a given materials system helps us to determine the dominant diffusion processes controlling the kinetics.

2.2.1 Nudged elastic band theory

A common problem in the study of kinetics is the identification of the lowest energy path when a group of atoms rearranges from one configuration to another. This path is often referred to as the minimum energy path (MEP). The potential energy maximum along the MEP is called the activation energy barrier, and it occurs at the saddle point. Many different techniques have been developed to study reaction pathways and to determine the activation energy barrier. NEB is one such method for finding saddle points and MEPs between known reactants and products. The method works by interpolating a set of images (configurations) between the known initial and final states, and then minimizing the energy of this string of images. This constrained optimization is done by adding spring forces along the band between images and by projecting out the component of the force due to the potential perpendicular to the band. Each image corresponds to a specific geometry of the atoms along the path from the initial to the final state. Once the energy of this string of images has been minimized, this string presents a candidate for the MEP.

2.2.2 Spin-polarized calculations

Materials can exhibit different types of magnetism, based on the configuration of spins in a material. Spin-polarized calculations within the framework of DFT are a powerful

tool to describe the magnetism of itinerant electrons in solid state materials. In cases where a material exhibits magnetism, VASP calculates a lower total energy for the spin-polarized state, implying that the material is more stable in this configuration.

2.3 Calculation details

Total energy calculations are carried out using VASP[10–13], within the framework of DFT. The gradient-corrected PBE exchange-correlation functional[21] is employed, along with the Projector Augmented Wave (PAW)[17,18] method. Calculations are carried out with periodic boundary conditions, with wave functions expanded on a plane-wave basis set. The *k*-point integration of the Brillouin zone is performed using a Monkhorst and Pack mesh.[22] Convergence calculations were performed to identify the required cut-off energy and size of the *k*-point mesh. For all our calculations, a 8×8×8 and 6×6×6 *k*-point mesh is employed for total energy and NEB calculations, respectively. The kinetic energy cutoff for the plane wave basis is set to 360 eV for total energy calculations, and 270 eV for NEB calculations. The corresponding cutoff energies for the augmentation functions are set to 650 eV and 480 eV. More details are given in the following sections.

2.3.1 Input files

INCAR: All energies were calculated at high precision, using the conjugate gradient algorithm. Partial occupancies were set using the tetrahedron method with Blöchl corrections.[17] The total energy convergence criterion was set to the default value of 5E-6 eV. The ISPIN tag was set to 2 or 1 based on whether the calculation was spin-polarized or not, respectively.

POTCAR: PAW-PBE potentials were used for all calculations. All POTCAR files were taken from the VASP library.

POSCAR: POSCAR files for all calculations were taken from the Naval Research Lab (NRL) website[23], or the Material Project website.[24,25] Super-cells were created, wherever necessary, using the program developed by another student in our group.

2.3.2 NEB calculations

NEB calculations are typically performed with lower energy cut-offs and a smaller *k*-point mesh (see Sec. 2.3). The spring constant is set to the default value of –5. We use 5 images for each of our energy barrier calculations, the two endpoints and three intermediate images.

2.3.3 Amorphous phase calculations

The 'melt-and-quench' method[26] is a common way to estimate the energies for amorphous phases, and it consists of using molecular dynamics (MD)[27] simulations to heat the system to a high temperature (above its melting point), and then gradually reducing the temperature. The resulting structure approximates an amorphous phase of the system, although the relatively short time scales accessible by MD during the cooling stage may mean that the similarity between the final structure and the real amorphous material – which in general has far longer to explore the local region of the potential energy surface – is limited. However, as an approximation to amorphous phases, the method seems reasonable and has been widely used.

We use a reduced energy cutoff of 200 eV, and a reduced convergence criterion for our MD calculations. The precision is set to ‘normal’, and the algorithm is set to ‘very fast’. The cell shape and volume, both, are allowed to vary during the calculation. The initial and final temperatures are determined based on the melting points of the systems under consideration. The time step and number of steps are varied to get a set of results, which are averaged to calculate the total energy of the amorphous phase.

CHAPTER 3

TRANSFORMATION OF COBALT TO COBALT OXIDE

3.1 Metal oxides

Most metals are easily oxidized, and this oxidation process is a simple method to synthesize metal oxides. The oxidation process is widely studied for bulk oxides, due to the dramatic change of properties as a metal transforms into a ceramic, but it is not well investigated for nanomaterials. Unlike bulk materials, NPs generally show size-dependent kinetics and thermodynamics.[28–30] Previous work on the oxidation of metal NPs – such as Ni-NiO,[31,32] Fe-Fe_xO_y,[33] and Co-CoO[34] – have yielded many important insights; however, the atomic structural evolutions and diffusion processes that occur during NP oxidation are not yet well understood.

3.1.1 Transition-metal oxides

Transition metal oxides are particularly interesting materials because they exhibit a wide range of properties. They may be dielectrics, semiconductors or metals; they exhibit unique magnetic and optical properties; they possess a variety of surface structures, which affect the surface energy of these compounds and influence their chemical properties, making them catalytically active. Cobalt oxides, in particular, have recently received increased attention due to their catalytic properties and potential as a promising anode material in Li-ion batteries.[35] Even though we know a lot about the structure, synthesis, and properties of these oxides, very little is known about the mechanisms and kinetics of the reaction that occurs as cobalt is oxidized.

3.1.2 Oxides of cobalt

As we have seen in Chapter 1, cobalt is known to exist in the ε-Co phase at the nanoscale. With oxygen, cobalt forms a series of compounds – CoO_2, Co_2O_3, CoO(OH), and Co_3O_4. However, cobalt oxides with an oxidation state of more than 3 are unstable in the natural environment,[36] and only CoO and Co_3O_4 occur as stable compounds. In air, Co first oxidizes to CoO, which then converts to Co_3O_4. Fig. 3.1 shows the Co-O phase diagram, indicating the stable phases.

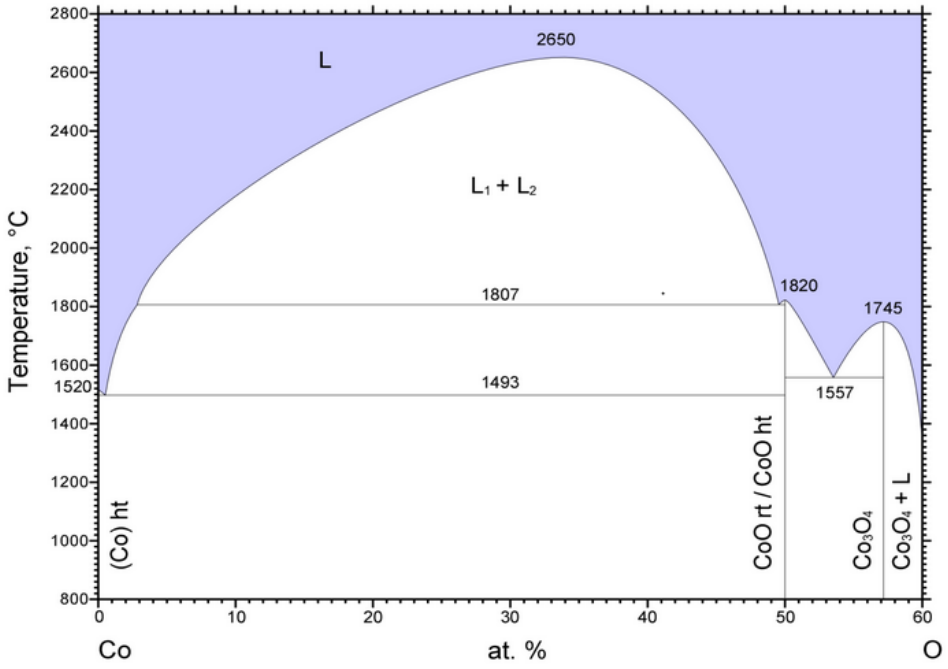

Figure 3.1. Binary phase diagram of the cobalt-oxide system. Concentration range: 0-60%. Temperature range: 800-2800°C.[37]

3.1.2.1 CoO

Cobalt (II) oxide, or cobalt monoxide, has a rock salt (NaCl) structure (a = 4.22 Å)[38] with cobalt at the corners and face centers of the cubic cell, and oxygen occupying the octahedral voids. Fig. 3.2 shows a unit cell of CoO. It is anti-ferromagnetic (below 16°C) and has a band gap of about 2.4 eV.[39]

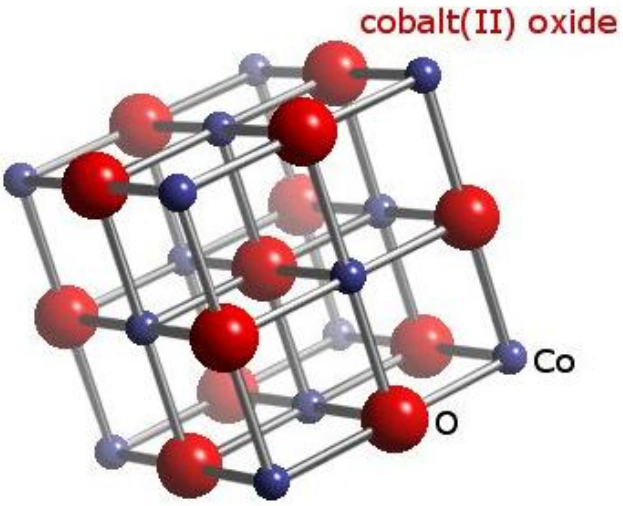

Figure 3.2. Unit cell of cobalt (II) oxide. Co atoms are in blue, O atoms are in red.[40]

3.1.2.2 Co_3O_4

Cobalt (II, III) oxide is a spinel tricobalt tetraoxide (a = 8.11 Å) with an energy band gap of 1.6 – 2.2 eV,[41] that can be used as a p-type semiconductor. It is also an anti-ferromagnetic material.[42] Co_3O_4 can be written as a mixed valence compound $CoO.Co_2O_3$ with Co^{2+} ions in tetrahedral interstices and Co^{3+} ions in octahedral interstices of the cubic close-packed lattice formed by the oxide anions (Fig. 3.3). It exhibits high catalytic activity and is finding increasing use in Li-ion batteries.[35]

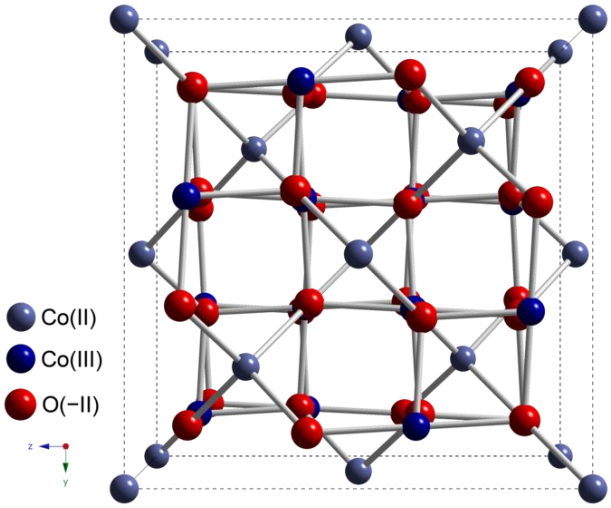

Figure 3.3. Unit cell of Co_3O_4. Co atoms are in blue, O atoms are in red.[40]

Here, we present a study of the chemical transformation of ε-Co metal into CoO and Co_3O_4, using DFT. In particular, in the cobalt to cobalt oxide transformation reaction, we seek to understand:

1. Kinetics of the nanoscale transformation
2. Diffusion processes during chemical conversion
3. Structural changes that occur during chemical transformation.

3.2 Calculation of diffusion activation barriers

3.2.1 ε-Co to CoO

To determine the diffusion activation energy for Co diffusing by a vacancy mechanism, we calculate first the vacancy formation energies for vacancies on sites I and II by removing a type I or II Co atom, respectively, from a 20-atom ε-Co cell. Using -

$$E_v^f = E[\varepsilon\text{-}Co_{19}V] - 19/20\ E[\varepsilon\text{-}Co_{20}],$$

the vacancy formation energies are found to be $E_{\varepsilon\text{-}Co19V(I)}^f$ = 1.39 eV and $E_{\varepsilon\text{-}Co19V(II)}^f$ = 1.84 eV. Since the energy for a vacancy in a type I site is lower than for a type II site, we expect that vacancies in ε-Co preferentially occupy type I sites. The type I sublattice forms a network of nearest neighbor sites such that it is possible for an atom to entirely diffuse through ε-Co on the type I site sublattice.

The migration energy barrier for a Co atom to move from a type I site to a neighboring vacant type I site, $E_{Co(I)\text{-}V(I)}^m$, is calculated using the NEB method. The initial path is obtained by a linear interpolation between the endpoint configurations. The resulting migration energy barrier is found to be only 0.08 eV. This gives a total activation energy, for Co atoms diffusing by vacancies on the type I subblattice, of $E_{Co(I)\text{-}V(I)}^{act}$ =

1.47 eV. This value is smaller than the vacancy formation energy on type II sublattice, indicating that in pure ε-Co diffusion on type I sublattice dominates.

O atoms in ε-Co can occupy either substitutional or interstitial lattice sites. Considering first substitutional defects, the formation energy for an ε-Co cell including a substitutional O atom on a Co site is calculated as follows –

$$E_{O(I)}^{f} = E[\varepsilon\text{-}Co_{19}O] - 19/20\ E[\varepsilon\text{-}Co_{20}] - \tfrac{1}{2}\ E[O_2]$$

It is found that $E_{O(I)}^{f} = -0.18$ eV for type I and $E_{O(II)}^{f} = 0.35$ eV for type II sites. The significantly lower formation energy for oxygen on type I sites compared to type II, indicates that oxygen atoms, just like vacancies, preferentially occupy type I lattice sites. For oxygen to diffuse to another type I site, it needs a vacancy in an adjacent site as well. Such a defect will have an energy given by -

$$E_{O(I)V(I)}^{f} = E[\varepsilon\text{-}Co_{18}O(I)V(I)] - 18/20\ E[\varepsilon\text{-}Co_{20}] - \tfrac{1}{2}\ E[O_2]$$

Calculating these energies for the type I sites, we obtain a defect formation energy of $E_{O(I)V(I)}^{f} = 1.02$ eV, indicating a small binding energy between O and vacancies. The barrier to migration for O into the neighboring vacant site is found to be $E_{O(I)\text{-}V(I)}^{m} = 0.21$ eV. This results in a final activation barrier of $E_{O(I)\text{-}V(I)}^{act} = 1.23$ eV.

To determine if O occupies interstitial sites in ε-Co, several interstitial sites were investigated. The most favorable site for the interstitial O atom in the 20-atom ε-Co cell is given by the fractional coordinates (0.375, 0.375, 0.375). Symmetrically equivalent positions within the cell are given by the fractional coordinates (0.875, 0.125, 0.625), (o.625, 0.875, 0.125) and (0.125, 0.625, 0.875). The formation energy of such a defect is calculated as –

$$E_{O(int)}^{f} = E[\varepsilon\text{-}Co_{20}O(int)] - E[\varepsilon\text{-}Co_{20}] - \tfrac{1}{2}\, E[O_2]$$

This result is $E_{O(int)}^{f} = -0.81$ eV. Using NEB, the migration energy barrier between adjacent interstitial sites in ε-Co is calculated to be $E_{O(int)\text{-}V(int)}^{m} = 2.53$ eV. The resulting diffusion activation barrier for interstitial diffusion of O is calculated to be $E_{O(int)\text{-}O(int)}^{act} = 1.72$ eV.

3.2.2 CoO to Co_3O_4

To study the transformation from CoO to Co_3O_4, vacancy mediated diffusion of Co and O in a 16-atom CoO cell is investigated. The formation energy of a Co vacancy in such a Co_8O_8 cell is calculated (using CoO and Co_3O_4 as references for chemical potentials) as -

$$E_{V(Co)}^{f} = E[\varepsilon\text{-}Co_7O_8] - \tfrac{1}{2}\, E[\varepsilon\text{-}Co_8O_8] - \tfrac{1}{2}\, E[\varepsilon\text{-}Co_6O_8]$$

Using this equation results in a formation energy of $E_{V(Co)}^{f} = 0.96$ eV. The barrier to migration of the Co atom is calculated using the NEB method as $E_{Co\text{-}V}^{m} = 0.18$ eV; the total diffusion activation barrier for Co is found to be $E_{Co\text{-}V}^{act} = 1.14$.

The diffusion activation barrier for O in CoO is calculated in a similar way.

$$E_{V(O)}^{f} = E[\varepsilon\text{-}Co_8O_7] - 1/20\, E[\varepsilon\text{-}Co_{20}] - 7/8\, E[\varepsilon\text{-}Co_8O_8]$$

The formation of a vacancy of the O sublattice is $E_{V(O)}^{f} = 1.14$ eV, using ε-Co and CoO for reference chemical potentials. Using NEB, the migration energy barrier for O to move to a neighboring vacant O sublattice site is found to be $E_{O\text{-}V}^{m} = 2.05$ eV. The diffusion activation barrier for O in CoO comes out to be $E_{O\text{-}V}^{act} = 3.19$ eV.

3.3 Discussion

3.3.1 ε-Co to CoO

Diffusion activation barriers are calculated for Co and O atoms diffusing through vacant sites in bulk ε-Co to infer the likely mechanism for the transformation from ε-Co to CoO. It is found that, for vacancy mediated diffusion, both Co and O atoms are more likely to diffuse through type I sites than type II sites, due to the lower formation energies of vacancies on type I sites. Activation barriers are also calculated for interstitial diffusion of O atoms through the bulk ε-Co crystal. Table 3.1 gives the formation energy, migration barrier and diffusion activation barrier for the diffusion of Co and O through bulk ε-Co.

For O in ε-Co, we observe that the defect formation energy is lower for an interstitial O atom than for O substituting a Co atom. However, the movement of such an interstitial atom is hindered by the high barrier towards migration. Oxygen vacancy diffusion seems most likely to dominate based on the comparison of the diffusion activation barriers.

Table 3.1. The formation energy, migration barrier and diffusion activation barrier for Co and O diffusing through ε-Co.

Diffusion type	Formation energy (eV)	Barrier to migration (eV)	Diffusion activation barrier (eV)
$Co_{(I)}$ - $V_{(I)}$	1.39	0.08	1.47
$O_{(I)}$ - $V_{(I)}$	1.02	0.21	1.23
$O_{(int)}$ - $O_{(int)}$	- 0.81	2.53	1.72

We investigated a number of complex diffusion pathways involving Co and O, as well, to infer the most likely mechanism for the transformation from ε-Co to CoO. We discovered a complex diffusion mechanism for O in ε-Co that is best described as an indirect-exchange mechanism illustrated in Fig. 3.4. First, a substitutional O atom on a type I site moves to an adjacent interstitial site with a small migration energy barrier. This step is followed by the migration of a neighboring Co atom into the now vacant type I site. Finally, the O atom migrates to the type I site abandoned by the moving Co atom. The diffusion activation barrier for the three-step mechanism is estimated by the highest energy barrier of the mechanism, and comes out to be 0.88 eV (Fig. 3.5). This diffusion migration energy barrier is considerably lower than for the vacancy-mediated diffusion of O and Co, respectively, through type I sites. In addition, this diffusion mechanism does not require the motion of Co vacancies. This indicates that O diffusion in ε-Co occurs via an indirect exchange mechanism of Co and O atoms.

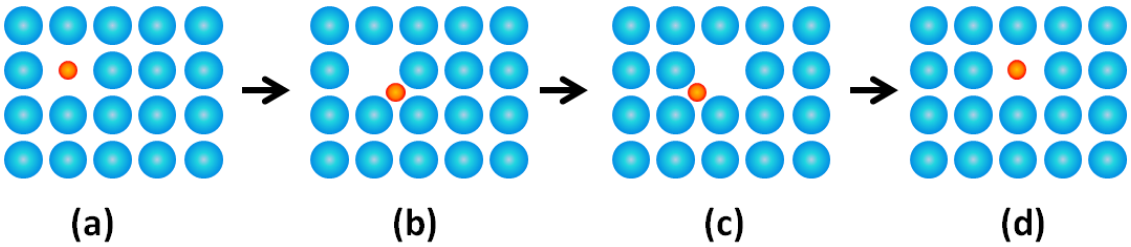

Figure 3.4. Schematic illustration of the proposed mechanism of O diffusion in the ε-Co phase taking place over three steps (a) – (d). (a) O atom in the vacant type I site; (b) O atom diffuses to an adjacent interstitial site; (c) neighboring type I Co atom diffuses to site vacated by O; (d) O hops back into the empty type I site.

3.3.2 CoO to Co_3O_4

Diffusion activation energies were also calculated for Co and O atoms diffusing by a vacancy mechanism in bulk CoO. The much lower activation energy for Co diffusion in CoO, compared to O, indicates that Co diffuses significantly faster than O in CoO.

Table 3.2 gives the formation energy, migration barrier and diffusion activation barriers for the diffusion of Co and O through CoO.

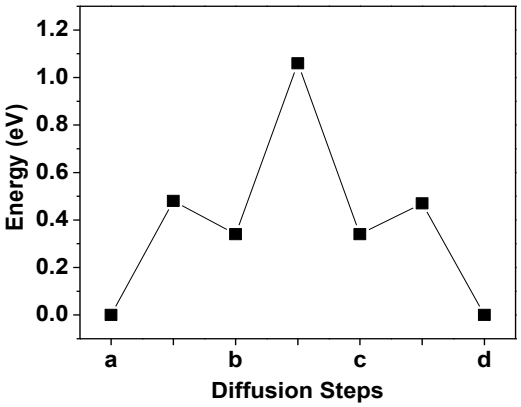

Figure 3.5. The migration energy diagram of the indirect-exchange mechanism.

Table 3.2.. The formation energy, migration barrier and diffusion activation barrier for Co and O diffusing through CoO.

Diffusion type	Formation energy (eV)	Barrier to migration (eV)	Diffusion activation energy (eV)
Co - V	0.96	0.18	1.14
O - V	1.14	2.05	3.19

3.4 Mechanism

The mechanism of the transformation from ε-Co to CoO can be described by combining the analyses and results from both experiments and calculations. The computational results suggest that the diffusional transformation from Co to Co_3O_4 occurs in two steps. First, O_2 reacts with ε-Co and diffuses into the ε-Co structure via the indirect-exchange mechanism, allowing O to enter the ε-Co NPs; once enough O is present, CoO is formed. Then, the diffusing mechanism switches, and Co diffuses faster in the CoO phase.

TEM, EXAFS and XRD results of our collaborators agree with this two step mechanism: No hollow structures were observed until 5 mins of the reaction (Fig. 3.6) meaning that O is still diffusing inward as fast as the outward Co diffusion. Once the major phase becomes CoO through 10 mins of the reaction, voids began to appear in the NP centers. This indicates that the Co diffusion is more rapid than the O diffusion, resulting in hollow structures. Therefore the change in the dominant diffusion mechanisms and rates of Co and O atoms occurs between 5 and 10 mins of the reaction. This insight into the nanoscale Kirkendall effect mirrors previous results in the Co-P system that showed a similar two-step process.[43]

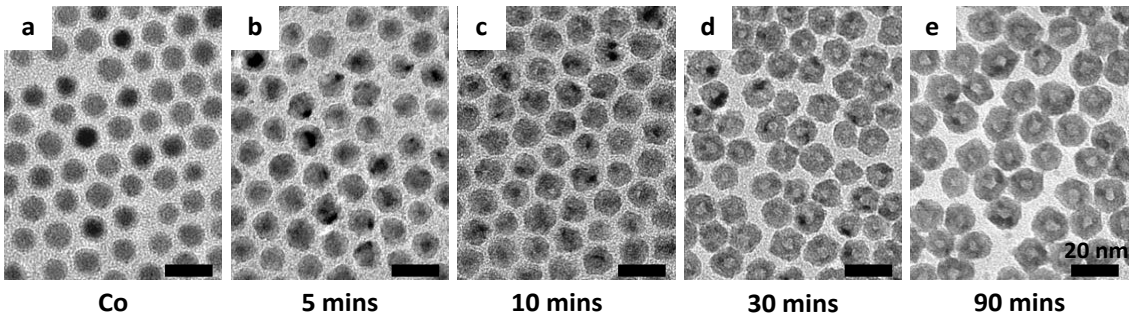

Figure 3.6. TEM images of the samples during the oxidation at 200^{o}C in the air. (a) The initial ε-Co NPs are spherical with an oxide shell. The samples are oxidized for 5 mins (b), 10 mins (c), 30 mins (d), and 90 mins (e) and transform to a hollow structure with irregular faceted morphology. (*Work done by collaborators*)

Furthermore, the DFT calculations show that the formation energy of an amorphous phase with the stoichiometry of CoO is only 0.06 eV/atom higher than that of crystalline CoO. This suggests that the transformation from Co to CoO might occur through the formation of an amorphous CoO region, which then converts to crystalline CoO. Evidence for this amorphous CoO is observed in the EXAFS and XRD data. For the partially oxidized samples at 0 minutes, the EXAFS analysis of our collaborators (Fig. 3.7) shows a significant number of CoO bonds while no evidence of the crystalline CoO phase exists in the XRD patterns.

The mechanism of the transition from CoO to Co_3O_4 is different from that of Co to CoO. Co atoms are the mobile species while the O anion sublattice is expected to remain rigid due to the low diffusion activation energy of Co atoms in the CoO phase (see Table 3.2). This mechanism is well confirmed by the TEM images showing no further hollowing process from CoO to Co_3O_4 samples, with a similar size of the voids. The slight increase in the overall size of the NPs during the transformation from CoO to Co_3O_4 might be due to the formation of more cobalt oxide on the surface from the change in stoichiometry between CoO and Co_3O_4, that is, the excess Co from the CoO migrates from the CoO to the outer surface and forms the more O-rich Co_3O_4 phase after being exposed to O atoms in the air. This also indicates that the CoO sample does not contain any more Co-rich phase inside the CoO NPs, which may cause further hollowing.

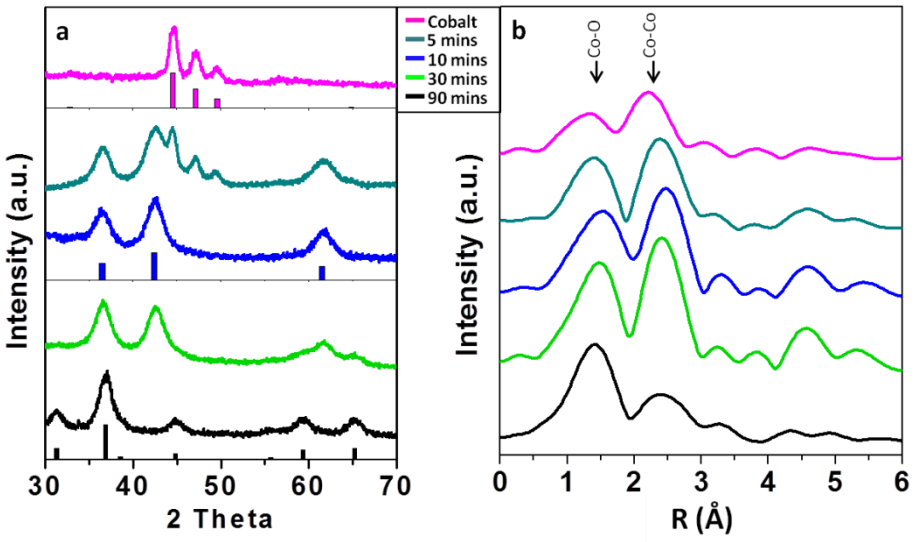

Figure 3.7. (a) XRD and (b) EXAFS results of the NP samples. The pink, turquoise, blue, light green, and black lines represent the starting cobalt NPs, oxidized for 5 mins, 10 mins, 30 mins, and 90 mins samples, respectively. The XRD patterns of the samples (left) during the oxidation show gradual transition from ε-Co phase (pink bars) to CoO (blue bars) and Co_3O_4 (black bars). (b) shows the corresponding fourier-transformed, k-weighted EXAFS data. (*Work done by collaborators*)

Combining XRD, EXAFS and TEM data with DFT calculations, we elucidate the atomic structural change and diffusion mechanisms during the oxidation from ε-Co to two phases (CoO and Co_3O_4) of cobalt oxide NPs. The initial ε-Co NPs likely form an amorphous CoO layer on the surface and this oxide layer grows (O diffusion inward) into the ε-Co NPs *via* an indirect-exchange mechanism. Once the crystalline CoO phase establishes, the Co atoms become the more mobile species, which leads to fast Co diffusion outwards and the formation of a void inside the cobalt oxide NPs.

CHAPTER 4

INDIRECT-EXCHANGE MECHANISM

In the previous chapter, we identified a new complex diffusion mechanism – the indirect-exchange mechanism – that has a lower diffusion activation barrier than any direct vacancy or interstitial diffusion mechanism. This three-step mechanism was one among various other complex diffusion mechanisms we studied. The low activation energy of the indirect-exchange mechanism results from the combination of the low defect formation energy with an intermediate migration energy barrier. To our knowledge, this is the first study of such a mechanism being predicted, and the question arises if a similar mechanism could occur in other materials as well.

4.1 Co-X (X=N, F, S) systems

In this chapter, we explore several other systems to identify if the indirect-exchange mechanism could be active in these materials. Focusing on systems similar to Co-O, we divide the search into two groups: one group is made up of cobalt compounds having anions similar in size to O, and the other group with anions having a similar chemistry as O. Specifically, we look at the Co-N and Co-F systems which have anions in the same period as O in the periodic table and hence a comparable size, and also at Co-S which has similar chemistry to Co-O, since O and S lie in the same group (Fig. 4.1).

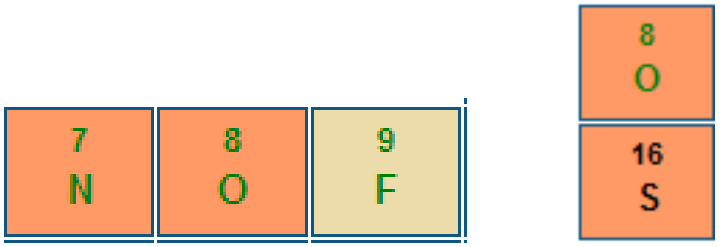

Figure 4.1. We pick cobalt nitrides, fluorides and sulfides for our study of the newly discovered indirect exchange mechanism.

For each of these systems, we calculate the diffusion activation barriers for vacancy and interstitial diffusion, and compare it to the values for the indirect-exchange mechanism, to predict which is most likely dominates the diffusion.

4.1.1 Co-N system

Cobalt forms three stable binary compounds with nitrogen, *viz.* Co_4N, Co_2N and CoN.[44–46] Co_4N has a cubic perovskite lattice structure (a = 3.74 Å) with one N atom located at the body center of an fcc-Co lattice. It is extensively used in the growth of single-crystal epitaxial films, and is considered a promising material for application to spintronic devices. While Co_2N possesses the orthorhombic Fe_2C structure, CoN exists in the more common zincblende structure.[44]

4.1.2 Co-F system

Cobalt reacts with fluorine to form a mixture of two stable compounds, cobalt (II) fluoride (CoF_2) and cobalt (III) fluoride (CoF_3). CoF_2 has a tetragonal structure, whereas the CoF_3 unit cell is hexagonal.[24] CoF_2 is a weak Lewis acid and a good reducing agent. CoF_3, on the other hand, is a powerful fluorinating agent that leaves CoF_2 as the by-product.

4.1.3 Co-S system

On reaction with sulfur, Co first forms the synthetic compound Co_9S_8.[47] Co also reacts to form CoS_2 and Co_3S_4 in the presence of excess sulfur. In combination with molybdenum, the sulfides of cobalt are used as catalysts for the industrial process

called hydrodesulfurization.[48] They react with strong acids to release hydrogen sulfide gas, and also act as weak reducing agents that can be oxidized to cobalt sulfate.

4.2 Calculation of diffusion activation barriers

Diffusion activation barriers for the three Co-X systems are calculated in a way similar to that in the Co-O system. The vacancy formation energy for Co diffusing through type I sites in ε-Co is calculated first. Adding the migration energy barrier for a Co atom to move from a type I site to a neighboring vacant type I site yields the diffusion activation energy for Co diffusion. X atoms in ε-Co can occupy either substitutional or interstitial lattice sites. Considering first substitutional defects, the formation energy for an ε-Co cell including a substitutional X atom on a Co site is calculated using a stable phase of X (N_2, F_2, S_8) to define the reference chemical potential. To determine if X can diffuse through Co vacancies, we calculate the formation energy for the defect pair of a substitutional X atom and a vacancy on a neighboring type I site. The NEB value for the migration energy barrier is added to give the resulting diffusion activation barrier for X atoms diffusing through vacancies. To study the case of interstitial diffusion, the formation energy of a defect with an X atom in the most favorable interstitial site is calculated. Using the NEB method, the migration energy barrier between adjacent interstitial sites in ε-Co is found, to give the final diffusion activation barrier for interstitial diffusion of X. Similarly, we also calculate the activation barrier for the indirect exchange mechanism in the Co-X systems by adding the formation energy of the initial defect and the migration barrier, estimated by the highest energy barrier of the mechanism.

4.3 Observations

Table 4.1 gives the formation energy, migration barrier and diffusion activation barrier for the diffusion of Co and X through ε-Co. The activation barriers from the Co-O system have been added for comparison. Kröger-Vink notation has been used.

Table 4.1. The formation energy, migration barrier and diffusion activation barrier for Co and X (X = O, N, F, S) diffusing through ε-Co.

Co-O

Diffusion type	Formation energy (eV)	Barrier to migration (eV)	Diffusion activation barrier (eV)
$Co_{Co}+V_{Co}$	1.39	0.08	1.47
Indirect	-0.18	1.06	0.88
$O_{Co}+V_{Co}$	1.02	0.21	1.23
Oi	-0.81	2.53	1.72

Co-N

Diffusion type	Formation energy (eV)	Barrier to migration (eV)	Diffusion activation barrier (eV)
$Co_{Co}+V_{Co}$	1.39	0.08	1.47
Indirect	1.51	0.89	2.40
$N_{Co}+V_{Co}$	2.33	0.28	2.61
Ni	-0.61	3.29	2.68

Co-F

Diffusion type	Formation energy (eV)	Barrier to migration (eV)	Diffusion activation barrier (eV)
$Co_{Co}+V_{Co}$	1.39	0.08	1.47
Indirect	0.38	1.83	2.21
$F_{Co}+V_{Co}$	1.10	0.18	1.28
Fi	-0.28	1.85	1.57

Co-S

Diffusion type	Formation energy (eV)	Barrier to migration (eV)	Diffusion activation barrier (eV)
$Co_{Co}+V_{Co}$	1.39	0.08	1.47
Indirect	0.21	1.68	1.89
$S_{Co}+V_{Co}$	1.26	0.21	1.47
Si	0.12	3.70	3.82

The first observation we make is that in none of the other systems is the activation barrier for 'indirect exchange' the lowest among all diffusion mechanisms, including the diffusion of Co. However, it is important to realize that 'Co-vacancy' values do not include any contributions from the reference energy terms (O_2, N_2, F_2, S_8), and hence remain constant throughout. The defect formation energies in all other cases are affected by the choice of our references. Hence, it is reasonable to exclude the 'Co-vacancy' from our considerations, for now. Looking at the tables without the 'Co-

vacancy' row, we can see that indirect-exchange is indeed the dominant mechanism in the Co-N system, apart from the Co-O system. Analyzing the numbers, individually, gives us an idea as to why it may or may not operate in the other systems. We can also make some general observations by comparing the numbers in the different systems against one another.

It can be seen that, in all four cases, the formation energy of a substitutional defect of an X atom on a Co site is less than the formation energy of a defect pair of a substitutional X atom and an adjoining vacancy ($E_{X(I)}^{f} < E_{X(I)V(I)}^{f}$). This observation reflects the high formation energy of Co vacancies. Overall, the defect formation energies follow the trend $E_{X(I)}^{f} < E_{X(I)V(I)}^{f} < E_{X(int)}^{f}$. This means that the formation energy of an interstitial X defect is the lowest.

However, interstitial diffusion in each case is hindered by the existence of a very high migration barrier. In fact, the migration energies for interstitial diffusion are the highest for any mechanism in all four systems. These migration energies can be seen to follow a trend based on the size of their anions ($E_{F(int)\text{-}V(int)}^{m} < E_{O(int)\text{-}V(int)}^{m} < E_{N(int)\text{-}V(int)}^{m} < E_{S(int)\text{-}V(int)}^{m}$).

The migration barrier energy for X diffusing through vacancies is very similar for all four systems ($E_{O(I)\text{-}V(I)}^{m}$ = 0.21 eV, $E_{N(I)\text{-}V(I)}^{m}$ = 0.28 eV, $E_{F(I)\text{-}V(I)}^{m}$ = 0.18 eV, $E_{S(I)\text{-}V(I)}^{m}$ = 0.21 eV). This could imply that the barrier to X movement on vacancies in ε-Co is size-independent.

In the Co-S system, particularly, where the size of the anion is the largest, we see that all mechanisms that require S to diffuse interstitially, have very high migration barriers, indicating that S movement through interstitial sites in ε-Co is greatly impeded due to its large size.

4.4 Discussion

Based on our observations, we can hazard a guess as to why the indirect-exchange mechanism might operate in some of these systems. We see that the formation of a vacancy on a ε-Co site is energetically unfavorable. At the same time, formation of an interstitial X defect is very favorable. Similarly, X finds it difficult to migrate interstitially, due to size constraints in the ε-Co cell, but prefers to migrate through vacancies on ε-Co sites, as can be seen from the low values of migration energy.

If we now look at the indirect-exchange mechanism, one step at a time, we see that it incorporates all the favorable entities we have talked about, leaving behind the ones that are unfavorable. Figure 4.2, showing the indirect-exchange, is the same one used in the previous chapter. We see that, in part (a), only a substitutional X atom exists, without any additional vacancy. As a result, the formation energy of such a defect is quite low. Subsequently, this X atom migrates into an interstitial site, which is favorable to form, compensating for the formation of the vacancy left behind. Also, the movement of atom X is not from one interstitial site to another, but from a substitutional site (a) to an interstitial site (b, c) to a vacancy (d). It, thus, encounters a small migration barrier, and has sufficient space to move to a neighboring site as its motion is not impeded by any neighboring Co atoms. As a whole, the entire mechanism is composed of the defects and paths that are energetically favorable. This makes it a 'low activation barrier' mechanism likely to be found in other material systems as well.

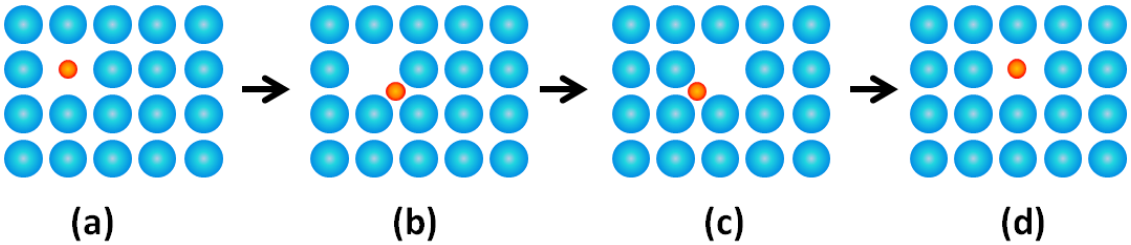

Figure 4.2. The proposed mechanism of X diffusion in the ε-Co phase taking place over three steps (a) – (d). (a) X atom in the vacant type I site; (b) X atom diffuses to an adjacent interstitial site; (c) neighboring type I Co atom diffuses to site vacated by X; (d) X hops back into the empty type I site.

Through this project, we have looked at an interesting complex diffusion mechanism that is likely to operate in the Co-O system, and possibly the Co-N system as well. By comparing the energies and barriers in a few different material systems, we are able to make some observations about the diffusion processes operating in these systems. With the help of these observations, we have tried to explain the reasons behind the likelihood of existence of the indirect-exchange mechanism. The discovery of such a mechanism, no doubt, is very exciting. The challenge, on our part, lies in identifying those systems where this mechanism might be found to operate.

CHAPTER 5

ANION EXCHANGE

Experimental characterization gives us information about structure, composition, bond distances etc. However, it doesn't tell us much about the thermodynamics behind the reaction or the kinetics involved in the transformation. It would be useful to combine experimental results with computational simulations to be able to predict the most likely mechanism for a reaction. Theoretical calculations can provide information about the energetics, atomistic structures of surfaces and diffusion barriers. DFT, in particular, provides an accurate and efficient method for the description of ground state properties of metals, semiconductors, and insulators, and has successfully been applied to many materials systems. Using DFT we can calculate the defect formation energies, migration energy barriers, and hence predict the diffusion activation energies that control the kinetics of phase transformation. Combining these values with XRD and XAS data helps us identify the diffusing species and thus elucidate the reaction pathways of the NPs during their chemical transformation.

5.1 Ion exchange reactions

Ion exchange has emerged as an effective approach for the synthesis of ionic NPs with novel structures and geometries, which are not accessible by conventional synthetic methods. Research in this field has mainly focused on cation exchange, that is, the cationic sublattice is replaced with a different metal ion while preserving the anionic framework. The anion exchange of NPs is less studied and only a few examples have been reported to date. The first report is from 2003,[49] in which ZnO was converted to ZnS by reacting with H_2S or elemental S at temperatures above 350^{o}C in the solid state.

More recently, Schaak[50] and Alivisatos[51] studied solution-processed anion exchange of colloidal NPs on the same ZnO/ZnS system, using thiourea and (trimethylsilyl) sulfide (TMS) as a sulfide reagent, respectively. Anion exchange was also used to produce several other semiconductor nanocrystals, including Cu_7S_4,[52] ZnSe,[53] and AlN.[54] Compared to cation exchange – which is fast and facile, and thus well developed – the reactivity of these reported anion-exchange reactions is much lower, and generally require higher temperatures (> 200^{o}C) or longer times (> 6h). The low reactivity of the anion exchange could be attributed to the lack of reactive anion reagents or the slow movement of the large anions in these ionic compounds.

Here, I present a study of the anion exchange reaction transforming colloidal CoO NPs to cobalt sulfide NPs. The experimental part of the project is carried out by our collaborators. Combining their results with our theoretical predictions, we are able to elucidate the mechanism for the studied anion exchange reaction.

5.2 Experimental work (carried out by collaborators)

$(NH_4)_2S$ is used as the reagent for the anion exchange reaction. Due to its ionic nature, $(NH_4)_2S$ can readily provide S^{2-} under ambient conditions. A 4:1 molar ratio of $(NH_4)_2S$ to CoO is used to fully convert hollow CoO NPs into amorphous cobalt sulfide particles with a Co:S ratio of 0.76:1, at a low temperature of 70^{o}C, in a few minutes. Crystalline cobalt sulfide NPs, with a major phase of Co_3S_4, are obtained by annealing amorphous NPs in an organic solution (Fig. 5.1).

The reaction with $(NH_4)_2S$ significantly changes the atomic structures of the initial CoO NPs. The X-ray powder diffraction (XRD) studies on the post-treated NPs reveal an amorphous phase, without any characteristics of the original CoO pattern (Figure 5.2).

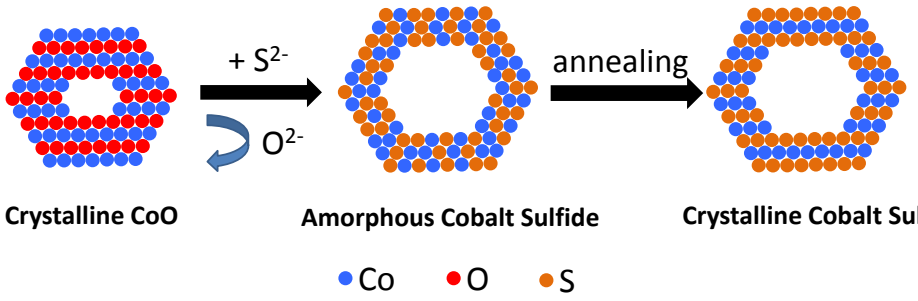

Figure 5.1. Schematic of chemical transformation from CoO to cobalt sulfide NPs.

The amorphous nature of the NPs is also confirmed by high-resolution transmission electron microscopy (HRTEM), which shows no long range atomic ordering. The starting CoO NPs have an average size of 14.4 ± 2.6 nm, with 6.3 ± 1.3 nm voids. The reaction with $(NH_4)_2S$ expands the void size to 11.9 ± 1.5 nm, and the overall NP size also slightly increases to 16.4 ± 2.0 nm. Inductively coupled plasma mass spectrometry (ICP-MS) analyses on the amorphous NPs gives a Co:S ratio of 0.76:1, confirming the incorporation of S^{2-} into NPs during reaction. Based on ICP-MS data, the amorphous cobalt sulfide NPs have a chemical composition of Co_3S_4, which indicated that 2/3 of Co^{2+} ions in the original CoO sample were oxidized to Co^{3+} during anion exchange reactions.

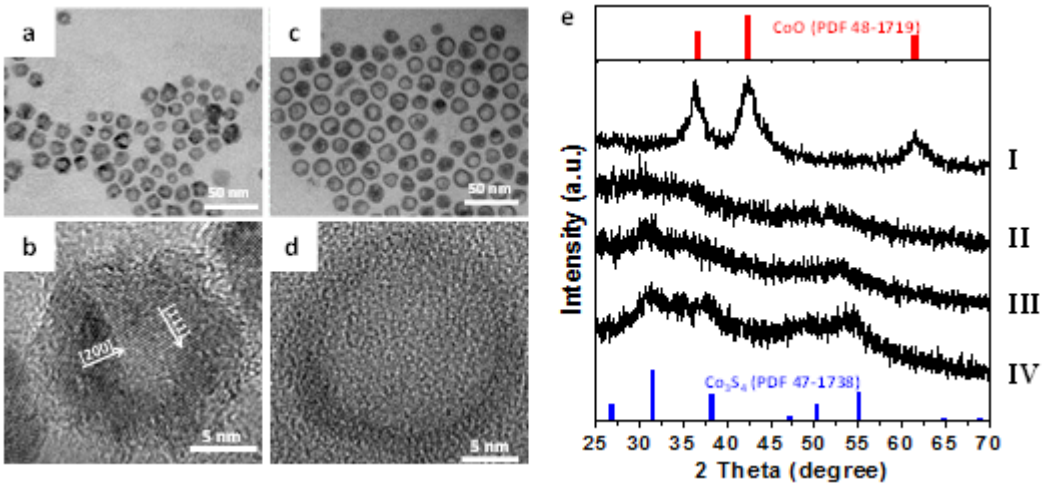

Figure 5.2.. TEM images of (a) CoO and (c) amorphous Co-S NPs. HRTEM images of (b) CoO and (d) amorphous Co-S NPs. (e) XRD patterns of (I) CoO NPs and Co-S NPs at different temperatures: (II) 70°C, (III) 100°C, (IV) 130°C. (*Work done by collaborators*)

TEM studies confirm that the NPs keep their original size and morphology after annealing (Figure 5.3a), and no decomposition is observed during the annealing process. HRTEM images also show the polycrystalline nature of cobalt sulfide NPs (Figure 5.3b).

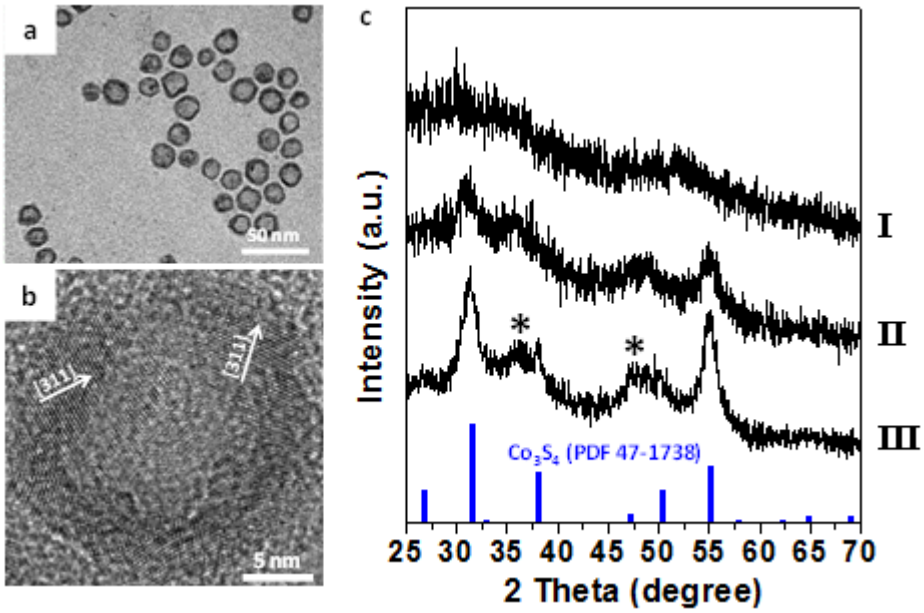

Figure 5.3. (a) TEM image of cobalt sulfide NPs obtained from annealing of amorphous Co-S NPs at 200 ^{o}C for 1 hour. (b) HRTEM image of polycrystalline cobalt sulfide NP, showing (311) facet of cubic Co_3S_4. (c) XRD patterns of cobalt sulfide NPs (I) before annealing and (II, III) after annealing. The blue stick pattern corresponds to cubic Co_3S_4. (*Work done by collaborators*)

5.3 Calculation of diffusion activation barriers

We calculate the diffusion activation barriers of Co, O and S atoms diffusing through the CoO phase, to identify the probable diffusion mechanisms in the Co-O-S system. The formation energy of a Co vacancy in a Co_8O_8 cell is calculated as –

$$E_{V(Co)}^{f} = E[\varepsilon\text{-}Co_7O_8] - \tfrac{1}{2}\, E[\varepsilon\text{-}Co_8O_8] - \tfrac{1}{2}\, E[\varepsilon\text{-}Co_6O_8]$$

Using the above equation, we get a defect formation energy of $E_{V(Co)}^{f}$ = 0.96 eV, using the energies of CoO and Co_3O_4 as reference chemical potentials. The barrier to migration of the Co atom is calculated using the NEB method as $E_{Co\text{-}V}^{m}$ = 0.18 eV; the total diffusion activation barrier for Co is found to be $E_{Co\text{-}V}^{act}$ = 1.14.

The diffusion activation barrier for O in CoO is calculated in a similar way.

$$E_{V(O)}^{f} = E[\varepsilon\text{-}Co_8O_7] - 1/20\ E[\varepsilon\text{-}Co_{20}] - 7/8\ E[\varepsilon\text{-}Co_8O_8]$$

The energy required to form an oxygen vacancy is found to be $E_{V(O)}^{f}$ = 1.14 eV, with the energies of ε-Co and CoO used as reference chemical potentials. Using NEB, the migration energy barrier for O to move to a neighboring vacant O sublattice site is found to be $E_{O\text{-}V}^{m}$ = 2.05 eV. The diffusion activation barrier for O in CoO comes out to be $E_{O\text{-}V}^{act}$ = 3.19 eV.

To find the diffusion activation barrier for S in CoO, we calculate the formation energy of a Co_8O_6SV cell, using the energies of ε-Co, CoO, O_2 and S as reference chemical potentials.

$$E_{S(O)V(O)}^{f} = E[\varepsilon\text{-}Co_8O_6SV] - 1/20\ E[\varepsilon\text{-}Co_{20}] - 6/8\ E[\varepsilon\text{-}Co_8O_8] - E[S]$$

The formation energy is calculated to be $E_{S(O)V(O)}^{f}$ = 3.08 eV. Adding the migration barrier of $E_{S\text{-}V}^{m}$ = 2.63 eV, calculated using NEB, to the defect formation energy gives us a final diffusion activation barrier of $E_{S\text{-}V}^{act}$ = 5.71 eV.

Table 5.1 summarizes the formation energies, migration barriers and diffusion activation barriers for the diffusion of Co, O and S atoms through the CoO crystal.

Table 5.1. The formation energy, migration barrier and diffusion activation barrier for Co, O and S diffusing through CoO.

Diffusion type	Formation energy (eV)	Barrier to migration (eV)	Diffusion activation barrier (eV)
Co diffusion	0.96	0.18	1.14
O diffusion	1.14	2.05	3.19
S diffusion	3.08	2.63	5.71

5.4 Discussion

Anion exchange reactions are quite rare in NPs due to the slow movement of the big anions. However, the CoO to Co_3S_4 transformation can be explained by the hard soft acid base (HSAB) theory. According to the HSAB theory, hard acids like hard bases, and soft acids like soft bases. Accordingly, Co^{2+} being a soft acid would like to interact with the soft base S^{2-} rather than the hard base O^{2-}. On reaction with a reactive reagent like $(NH_4)_2S$, CoO readily gives up its O^{2-} to form Co_3S_4, as observed by our collaborators.

The diffusion activation barriers for Co, O and S in CoO give an indication of the mechanism of the reaction. Sulfur, having the largest activation barrier, does not diffuse any appreciable distance but reacts with the surface layer of the CoO NPs. Co, on the other hand, and O (to some extent) diffuse outwards faster than the incoming S. This results in further Kirkendall hollowing of the already hollow NP, which explains the increasing void size and increasing NP size in the TEM image (Fig. 5.2).

The formation of Co_3S_4 could possibly be explained by the large ratio (4:1) of $(NH_4)_2S$ to CoO precursor. CoO would be expected to react with S^{2-} to form Co_9S_8 because it has a Co:S ratio (9:8) closer to the Co:O ratio in CoO (1:1). However, the high initial concentration of S^{2-} would tend to favor the formation of Co_3S_4, as detected in the XRD images.

MD simulations carried out to find the energy of the amorphous $Co_{0.75}S$ yielded a value 0.14 eV/atom above the crystalline Co_3S_4 structure. This low formation energy, combined with the extremely low mobility of sulphur, might explain the formation of the amorphous phase, which can subsequently be annealed to give Co_3S_4. Since the movement of anions is hindered by their large size, a higher barrier exists for the structural rearrangement as $Co_{0.75}S$ transforms to Co_3S_4. Annealing provides energy necessary to overcome this barrier and transform to the more stable crystalline structure.

We have thus combined theoretical and experimental results to explain the kinetics and diffusion processes involved in the anion exchange reaction converting metal oxide NPs to metal sulfides NPs. $(NH_4)_2S$ exhibits a high reactivity, converting the CoO NPs into amorphous cobalt sulfide NPs at low temperature (70 °C) in only a few minutes. Annealing of these amorphous NPs in an organic solution produced polycrystalline cobalt sulfide NPs, and Co_3S_4 was identified as the major phase. Characterization tools like TEM and XRD coupled with our DFT calculations helped us figured out the most likely mechanism for this transformation.

CHAPTER 6

CONCLUSION

With the help of DFT, we studied the kinetics of the transformation of ε-cobalt to its oxides and sulfides. The calculated defect formation energies and migration energy barriers from the nudged elastic band method were combined to determine the diffusion activation energies. Comparing these activation barriers for various diffusing species and pathways helped us predict the diffusion mechanisms of the oxidation and anion exchange reactions.

For the Co-O system, we concluded that the diffusional transformation from Co to Co_3O_4 occurs in two steps. Initially, O diffuses rapidly into the ε-Co structure, and Co diffuses out, *via* the indirect-exchange mechanism. Once enough O is present in the cobalt, CoO is formed. In the newly formed CoO phase, Co becomes the fast diffusing species. Furthermore, calculations of the formation energy of the amorphous CoO phase indicated that the transformation from Co to CoO might occur through the formation of an amorphous CoO region, which then converts to crystalline CoO. The mechanism of the transition from CoO to Co_3O_4 is different from that of Co to CoO. Co atoms are the mobile species, while the O anion sublattice is expected to remain rigid, due to the lower diffusion activation energy of Co atoms in the CoO phase.

While carrying out calculations on the Co-O system, we came across an exciting complex indirect-exchange mechanism. We studied several related systems to identify other materials where such a diffusion mechanism could be active. Based on our calculations, we made several interesting observations that helped us explain the science behind the indirect-exchange mechanism, and also identify another material, the

Co-N system, where the indirect-exchange mechanism likely dominates the anion diffusion.

In our final project, we looked at the anion-exchange reaction, transforming CoO to Co_3S_4. We used DFT calculations in combination with experimental results from our collaborators to explain the diffusion processes involved in the reaction.

Throughout this project, we have seen that combining experimental results and theoretical predictions can help us study transformation reactions at the nanoscale. Theoretical calculations provide the fundamental details of phase stability, diffusion pathways, and diffusion activation energies, which combined with experimental synthesis efforts and characterization techniques provide a detailed picture of the structural changes that occur during the transformation reactions. Knowledge about the transformation mechanism and the structural properties of these materials provides a means to control the synthesis and composition of the NPs and facilitate the optimization of such NPs for use in applications.

REFERENCES

1. Yin, Y. *et al.* Formation of hollow nanocrystals through the nanoscale Kirkendall effect. *Science* **304**, 711–714 (2004).

2. Fan, H. J., Gösele, U. & Zacharias, M. Formation of nanotubes and hollow nanoparticles based on Kirkendall and diffusion processes: a review. *Small Weinheim an der Bergstrasse Germany* **3**, 1660–1671 (2007).

3. Superlattices, C. S. N. *et al.* Formation Mechanism and Properties of. *ACS Nano* **2**, 627–636 (2008).

4. Crystallography tutorial. *University of Southhampton* at <http://www.southampton.ac.uk/~engmats/xtal/diffusi>

5. Janak, J. F. (IBM) Itinerant Ferromagnetism in FCC Cobalt. *Solid State Communications* **25**, 53–55 (1978).

6. Cobalt (Co). *Encyclopaedia Brittanica Online* (2013).at <http://www.britannica.com/>

7. Dinega, D. P. & Bawendi, M. G. A Solution-Phase Chemical Approach to a New Crystal Structure of Cobalt. *Angewandte Chemie International Edition* **38**, 1788–1791 (1999).

8. Hohenberg, P. & Kohn, W. Inhomogeneous Electron Gas. *Physical Review* **136**, B864–B871 (1964).

9. Kohn, W. & Sham, L. J. Self-Consistent Equations Including Exchange and Correlation Effects. *Physical Review* **140**, A1133–A1138 (1965).

10. Kresse, G. & Hafner, J. Ab initio molecular dynamics for liquid metals. *Physical Review B* **47**, 558–561 (1993).

11. Kresse, G. & Hafner, J. Ab initio molecular-dynamics simulation of the liquid-metal-amorphous-semiconductor transition in germanium. *Physical Review B* **49**, 14251–14269 (1994).

12. Kresse, G. Efficiency of ab-initio total energy calculations for metals and semiconductors using a plane-wave basis set. *Computational Materials Science* **6**, 15–50 (1996).

13. Kresse, G. & Furthmüller, J. Efficient iterative schemes for ab initio total-energy calculations using a plane-wave basis set. *Physical review B Condensed matter* **54**, 11169–11186 (1996).

14. Vanderbilt, D. Optimally smooth norm-conserving pseudopotentials. *Physical Review B* **32**, 8412–8415 (1985).

15. Vanderbilt, D. Soft self-consistent pseudopotentials in a generalized eigenvalue formalism. *Physical Review B* **41**, 7892–7895 (1990).

16. Laasonen, K., Car, R., Lee, C. & Vanderbilt, D. Implementation of ultrasoft pseudopotentials in ab initio molecular dynamics. *Physical Review B* **43**, 6796–6799 (1991).

17. Blöchl, P. E. Projector augmented-wave method. *Physical Review B* **50**, 17953–17979 (1994).

18. Kresse, G. & Joubert, D. From ultrasoft pseudopotentials to the projector augmented-wave method. *Physical Review B* **59**, 1758–1775 (1999).

19. University of Tennessee: Introduction to Materials Science. at <http://web.utk.edu/~prack/mse201/Chapter 5 Diffusion .pdf>

20. Jónsson, H., Mills, G. & Jacobsen, K. W. Nudged elastic band method for finding minimum energy paths of transitions. *Classical and Quantum Dynamics in Condensed Phase Simulations Proceedings of the International School of Physics* 385–404 (1998).doi:10.1142/9789812839664_0016

21. Perdew, J., Burke, K. & Ernzerhof, M. Generalized Gradient Approximation Made Simple. *Physical Review Letters* **77**, 3865–3868 (1996).

22. Monkhorst, H. J. & Pack, J. D. Special points for Brillouin-zone integrations. *Physical Review B* **13**, 5188–5192 (1976).

23. Naval Reserach Laboratory wesite. at <http://www.nrl.navy.mil/>

24. S. P. Ong, A. Jain, G. Hautier, M. Kocher, S. Cholia, D. Gunter, D. Bailey, D. Skinner, K. Persson, G. C. The Materials Project. *The Materials Project* at <http://materialsproject.org/>

25. Jain, A. *et al.* A high-throughput infrastructure for density functional theory calculations. *Computational Materials Science* **50**, 2295–2310 (2011).

26. Evgueni A Chagarov, A. C. K. Generation of Realistic Amorphous Al2O3 And ZrO2 Samples By Hybrid Classical and First-Principle Molecular Dynamics Simulations. *ECS Transactions* **16**, 773–785 (2008).

27. Alder, B. J. & Wainwright, T. E. Studies in Molecular Dynamics. I. General Method. *The Journal of Chemical Physics* **31**, 459 (1959).

28. Navrotsky, A., Ma, C., Lilova, K. & Birkner, N. Nanophase transition metal oxides show large thermodynamically driven shifts in oxidation-reduction equilibria. *Science* **330**, 199–201 (2010).

29. Guisbiers, G. Schottky Defects in Nanoparticles. *The Journal of Physical Chemistry C* **115**, 2616–2621 (2011).

30. Barnard, A. S. Direct Comparison of Kinetic and Thermodynamic Influences on Gold Nanomorphology. *Accounts of Chemical Research* **XXX**, 120615101540000 (2012).

31. Nakamura, R., Lee, J.-G., Mori, H. & Nakajima, H. Oxidation behaviour of Ni nanoparticles and formation process of hollow NiO. *Philosophical Magazine* **88**, 257–264 (2008).

32. Railsback, J. G., Johnston-Peck, A. C., Wang, J. & Tracy, J. B. Size-dependent nanoscale kirkendall effect during the oxidation of nickel nanoparticles. *ACS nano* **4**, 1913–1920 (2010).

33. Cabot, A. *et al.* Vacancy coalescence during oxidation of iron nanoparticles. *Journal of the American Chemical Society* **129**, 10358–10360 (2007).

34. Jia, S., Hsia, C.-H. & Son, D. H. In Situ Study of Room-Temperature Oxidation Kinetics of Colloidal Co Nanocrystals Investigated by Faraday Rotation Measurement. *The Journal of Physical Chemistry C* **115**, 92–96 (2011).

35. Wu, Z.-S. *et al.* Graphene anchored with co(3)o(4) nanoparticles as anode of lithium ion batteries with enhanced reversible capacity and cyclic performance. *ACS nano* **4**, 3187–3194 (2010).

36. Tang, C.-W., Wang, C.-B. & Chien, S.-H. Characterization of cobalt oxides studied by FT-IR, Raman, TPR and TG-MS. *Thermochimica Acta* **473**, 68–73 (2008).

37. Chen, M., Hallstedt, B. & Gauckler, L. J. Thermodynamic assessment of the Co-O system. *Journal of Phase Equilibria* **24**, 212–227 (2003).

38. Seehra, R. K. and M. S. Percolation effects and magnetic properties of the randomly diluted fcc system CopMg1-pO. *Physical Review B* **35**, 6847–6853 (1987).

39. Silinsky, P. & Seehra, M. Principal magnetic susceptibilities and uniaxial stress experiments in CoO. *Physical Review B* **24**, 419–423 (1981).

40. Winter Mark (The University of Sheffield and WebElements Ltd UK) WebElements: the periodic table on the WWW. (1993).at <http://www.webelements.com/>

41. Varghese, B. *et al.* Electrical and photoresponse properties of Co3O4 nanowires. *Journal of Applied Physics* **111**, 104306 (2012).

42. Xu, X., Chen, Z., Li, Y., Chen, W. & Li, J. Bulk and surface properties of spinel Co3O4 by density functional calculations. *Surface Science* **603**, 653–658 (2009).

43. Ha, D.-H. *et al.* The structural evolution and diffusion during the chemical transformation from cobalt to cobalt phosphide nanoparticles. *Journal of Materials Chemistry* **21**, 11498 (2011).

44. Matar, S. F., Houari, A. & Belkhir, M. A. Ab initio studies of magnetic properties of cobalt and tetracobalt nitride Co4N. *Physical Review B* **24**, 1–19 (2007).

45. Oda, K., Yoshio, T. & Oda, K. Preparation of Co-N films by rf-sputtering. *Journal of Materials Science* **22**, 2729–2733 (1987).

46. Hasegawa, M. & Yagi, T. Synthesis of Co2N by a simple direct nitriding reaction between nitrogen and cobalt under 10GPa and 1800K using diamond anvil cell and YAG laser heating. *Solid State Communications* **135**, 294–297 (2005).

47. Chauke, H. R., Nguyen-Manh, D., Ngoepe, P. E., Pettifor, D. G. & Fries, S. G. Electronic structure and stability of the pentlandites Co9S8 and (Fe,Ni)(9)S-8. *Physical Review B* **66**, 1–5 (2002).

48. Kubota, T., Okamoto, H. & Okamoto, Y. Hydrodesulfurization activity of highly dispersed Co sulfide clusters prepared in zeolite cages. *Catalysis Letters* **67**, 171–174 (2000).

49. Dloczik, L. & Ko, R. Nanostructure Transfer in Semiconductors by Ion Exchange. *Nano letters* 4–6 (2003).

50. Dawood, F. & Schaak, R. E. ZnO-templated synthesis of wurtzite-type ZnS and ZnSe nanoparticles. *Journal of the American Chemical Society* **131**, 424–5 (2009).

51. Jungwon Park , Haimei Zheng, Young-wook Jun, A. P. A. Hetero-Epitaxial Anion Exchange Yields Single-Crystalline Hollow Nanoparticles. *Journal of the American Chemical Society* **131**, 13943 (2009).

52. Cao, H. *et al.* High symmetric 18-facet polyhedron nanocrystals of Cu7S4 with a hollow nanocage. *Journal of the American Chemical Society* **127**, 16024–5 (2005).

53. Geng, J., Liu, B., Xu, L., Hu, F.-N. & Zhu, J.-J. Facile route to Zn-based II-VI semiconductor spheres, hollow spheres, and core/shell nanocrystals and their optical properties. *Langmuir : the ACS journal of surfaces and colloids* **23**, 10286–93 (2007).

54. Zhang, Q. & Gao, L. Synthesis of Nanocrystalline Aluminum Nitride by Nitridation of delta-Al2O3 Nanoparticles in Flowing Ammonia. *Journal of the American Ceramic Society* **89**, 415–421 (2006).